

# Photomechanical response of composites based on PDMS and carbon soot nanoparticles under IR laser irradiation

F. M. Sánchez-Arévalo,<sup>1,\*</sup> I. M. Garnica-Palafox,<sup>1,2</sup> P. Jagdale,<sup>3</sup> J. Hernández-Cordero,<sup>1</sup> S. E. Rodil,<sup>1</sup> A. O. Okonkwo,<sup>4</sup> F. C. Robles Hernandez<sup>4</sup> and A. Tagliaferro<sup>3</sup>

<sup>1</sup>*Instituto de Investigaciones en Materiales, Universidad Nacional Autónoma de México  
Apdo. Postal 70-360, Cd. Universitaria, D.F. 04510, México*

<sup>2</sup>*Posgrado en Ciencia e Ingeniería de Materiales, Universidad Nacional Autónoma de México  
Apdo. Postal 70-360, Cd. Universitaria, D.F. 04510, México*

<sup>3</sup>*Department of Applied Science and Technology (DISAT), Polytechnic of Turin, Turin-10129,  
Italy*

<sup>4</sup>*Mechanical Engineering Technology Department, College of Technology, University of  
Houston, Texas 77204-4020 USA*

[\\*fsanchez@iim.unam.mx](mailto:fsanchez@iim.unam.mx)

**Abstract:** We demonstrate a new type of smart composite based on carbon soot nanoparticles (CSP) and Poly(dimethylsiloxane). The addition of CSP in this polymeric matrix yields a composite with photomechanical response triggered by IR laser irradiation. The load capacity of this optically driven material ranged between 10 and 16 kPa depending on the CSP concentration in the composites. These photomechanical actuation features promises a good alternative for low-cost smart composite materials for photonic applications such as optically reconfigurable surfaces and optical actuating-sensing devices.

© 2015 Optical Society of America

**OCIS codes:** (160.3380) Laser materials; (160.5335) Photosensitive materials; (250.2080) Polymer active devices; (350.5340) Photothermal effects.

---

## References and links

1. A. G. Bell, "On the production and reproduction of sound by light" *Proc. Am. Assoc. Adv. Sci.* **29**, 115–136 (1881).
2. K. Uchino, "Ceramic actuators: principles and applications," *MRS Bull.* **29**, 42–48 (1993).
3. D. J. Welker and M. G. Kuzyk, "Photomechanical stabilization in a polymer fiber-based all-optical circuit," *Appl. Phys. Lett.* **64**, 809–811 (1994).
4. D. J. Welker and M. G. Kuzyk, "Suppressing vibrations in a sheet with a Fabry-Perot photomechanical device," *Opt. Lett.* **64**, 417–418 (1997).
5. H. Lu, Y. Liu, J. Gou, J. Leng, and S. Du, "Synergistic effect of carbon nanofiber and carbon nanopaper on shape memory polymer composite," *Appl. Phys. Lett.* **96**, 084102 (2010).
6. L. Sun, W. Huang, Z. Ding, Y. Zhao, C. Wang, H. Purnawali, and C. Tang, "Stimulus-responsive shape memory materials: A review," *Mater. Des.* **33**, 577 – 640 (2012).
7. J. Wang, Z. Chen, M. Mauk, K.-S. Hong, M. Li, S. Yang, and H. Bau, "Self-actuated, thermo-responsive hydrogel valves for lab on a chip," *Biomed. Microdevices* **7**, 313–322 (2005).
8. R. Geryak and V. V. Tsukruk, "Reconfigurable and actuating structures from soft materials," *Soft Matter* **10**, 1246–1263 (2014).
9. N. J. Dawson, M. G. Kuzyk, J. Neal, P. Luchette and P. Palffy-Muhoray, "Modeling the mechanisms of the photomechanical response of a nematic liquid crystal elastomer," *J. Opt. Soc. Am. B* **28**, 2134–2141 (2011).

10. N. J. Dawson, M. G. Kuzyk, J. Neal, P. Luchette, and P. Palffy-Muhoray, "Cascading of liquid crystal elastomer photomechanical optical devices," *Opt. Commun.* **284**, 991–993 (2011).
11. J. Hu, Y. Zhu, H. Huang, and J. Lu, "Recent advances in shapememory polymers: Structure, mechanism, functionality, modeling and applications," *Prog. Polym. Sci.* **37**, 1720–1763 (2012).
12. A. C. Kuo, "Poly (dimethylsiloxane)," *Polymer data handbook* pp. 411–435 (1999).
13. A. Mata, A. Fleischman, and S. Roy, "Characterization of polydimethylsiloxane (pdms) properties for biomedical micro/nanosystems," *Biomed. Microdevices* **7**, 281–293 (2005).
14. Y. Jiang, H. Wang, S. Li, and W. Wen, "Applications of micro/nanoparticles in microfluidic sensors: A review," *Sensors* **14**, 6952–6964 (2014).
15. S. Stassi, V. Cauda, G. Canavese, and C. F. Pirri, "Flexible tactile sensing based on piezoresistive composites: A review," *Sensors* **14**, 5296–5332 (2014).
16. J.-H. Kong, N.-S. Jang, S.-H. Kim, and J.-M. Kim, "Simple and rapid micropatterning of conductive carbon composites and its application to elastic strain sensors," *Carbon* **77**, 199 – 207 (2014).
17. F. Ataollahi, S. Pramanik, A. Moradi, A. Dalilottojari, B. Pinguan-Murphy, W. A. B. Wan Abas, and N. A. Abu Osman, "Endothelial cell responses in terms of adhesion, proliferation, and morphology to stiffness of polydimethylsiloxane elastomer substrates," *J. Biomed. Mater. Res. A* pp. n/a–n/a (2014).
18. J. Loomis, B. King, T. Burkhead, P. Xu, N. Bessler, E. Terentjev, and B. Panchapakesan, "Graphene-nanoplatelet-based photomechanical actuators," *Nanotechnology* **23**, 045501 (2012).
19. Y. Feng, N. Dong, Y. Li, X. Zhang, C. Chang, S. Zhang, and J. Wang, "Host matrix effect on the near infrared saturation performance of graphene absorbers," *Opt. Mater. Express* **5**, 802–808 (2015).
20. S. Ahir, Y. Huang, and E. Terentjev, "Polymers with aligned carbon nanotubes: Active composite materials," *Polymer* **49**, 3841–3854 (2008).
21. R. Pimentel-Domínguez, F. Sánchez-Arévalo, M. Hautefeuille, and J. Hernández-Cordero, "Laser induced deformation in polydimethylsiloxane membranes with embedded carbon nanopowder," *Smart Mater. Struct.* **22**, 037001 (2013).
22. P. R. Buseck, K. Adachi, A. Gelencsér, E. Tompa, and M. Pósfai, "Are black carbon and soot the same?," *Atmos. Chem. Phys. Discuss.*, **12**, 24821–24846 (2012).
23. M. I. Shahzad, M. Giorcelli, N. Shahzad, S. Guastella, M. Castellino, P. Jagdale, and A. Tagliaferro, "Study of carbon nanotubes based polydimethylsiloxane composite films," *J. Phys.: Conf. Ser.* **439**, 012010 (2013).
24. R. W. Ogden, "Large deformation isotropic elasticity - on the correlation of theory and experiment for incompressible rubberlike solids," *Proceedings of the Royal Society of London. A. Mathematical and Physical Sciences* **326**, 565–584 (1972).
25. H. F. Brinson and L. C. Brinson, *Polymer Engineering Science and Viscoelasticity: An Introduction* (Springer, 2007).
26. R. W. Ogden, G. Saccomandi, and I. Sgura, "Fitting hyperelastic models to experimental data," *Comput. Mech.* **34**, 484–502 (2004).
27. F. M. Sánchez-Arévalo and G. Pulos, "Use of digital image correlation to determine the mechanical behavior of materials," *Mater. Charact.* **59**, 1572–1579 (2008).
28. F. M. Sánchez-Arévalo, T. García-Fernández, G. Pulos, and M. Villagran-Muniz, "Use of digital speckle pattern correlation for strain measurements in a CuAlBe shape memory alloy," *Mater. Charact.* **60**, 775–782 (2009).
29. G. L. Jadv, V. K. Aswal, H. Bhatt, J. C. Chaudhari, and P. S. Singh, "Influence of film thickness on the structure and properties of PDMS membrane," *J. Membrane Sci.* **415416**, 624–634 (2012).
30. Z. Wen, Q. Wang, and J. Li, "Template synthesis of aligned carbon nanotube arrays using glucose as a carbon source: Pt decoration of inner and outer nanotube surfaces for fuel-cell catalysts," *Adv. Funct. Mater.* **18**, 959–964 (2008).
31. X. Feng, J. Hu, X. Chen, J. Xie, and Y. Liu, "Synthesis and electron transfer property of sulfhydryl-containing multi-walled carbon nanotube/gold nanoparticle heterojunctions," *J. Phys. D. Appl. Phys.* **42**, 042001 (2009).
32. S. Sagar, N. Iqbal, and A. Maqsood, "Dielectric, electric and thermal properties of carboxylic functionalized multi-walled carbon nanotubes impregnated polydimethylsiloxane nanocomposite," *J. Phys.: Conf. Ser.* **439**, 012024 (2013).
33. A. M. Alshehri, K. L. N. Deepak, D. T. Marquez, S. Desgreniers, and V. R. Bhardwaj, "Localized nanoclusters formation in pdms upon irradiation with femtosecond laser," *Opt. Mater. Express* **5**, 858–869 (2015).
34. P.-C. Ma, N. A. Siddiqui, G. Marom, and J.-K. Kim, "Dispersion and functionalization of carbon nanotubes for polymer-based nanocomposites: A review," *Compos. Part A-Appl. S.* **41**, 1345–1367 (2010).
35. J. R. Vélez-Cordero, J. Hernández-Cordero, "Heat generation and conduction in PDMS-carbon nanoparticle membranes irradiated with optical fibers," *Int. J. Therm. Sci.* **96**, 12–22 (2015).
36. I. D. Johnston, D. K. McCluskey, C. K. L. Tan, and M. C. Tracey, "Mechanical characterization of bulk sylgard 184 for microfluidics and microengineering," *J. of Micromech. Microeng.* **24**, 035017 (2014).

## 1. Introduction

Photomechanical response has been a subject of interest since 1881 when Alexander Graham Bell demonstrated that voice could be transmitted using a beam of light [1]. Since then, interesting applications based on this phenomenon have been demonstrated, such as the “Uchino walker” [2], which is based on ceramics that constrict when exposed to light and relax in the dark. Other interesting applications include Fabry-Perot photomechanical devices to suppress vibrations in a stretched plastic sheet [4] and photomechanical stabilizers for fiber-based optical circuits [3].

Recent efforts in smart materials have been devoted to produce reconfigurable polymers capable to perform stimuli-sensing, multi-length scale actuation or programmed shape control tasks [5–8]. These reconfigurable materials include azo-dye-doped liquid crystal elastomers [9, 10], as well as block copolymers showing shape memory effect such as polyethylene terephthalate- polyethyleneoxide, polystyrene-poly(1,4-butadiene) [11]. Poly(dimethylsiloxane) (PDMS) has also been used to produce smart composites, owing to its thermal, rheological, mechanical and biological properties [12, 13]. This has led to PDMS-based composites for microfluidics, engineering, medicine and biology fields [14–17].

Applications for PDMS-based sensors and actuator devices are mostly limited due to the inherent properties of this elastomeric material. Nonetheless, these limiting issues can be addressed by adding microparticles or nanoparticles of other materials as fillers. Different filling particles can be added to PDMS thus modifying properties such as conductivity, stiffness, or even its biological response [14–17]. As an example, aluminum oxide microparticles have been used to produce stiffer PDMS composites yielding improved performance for cell proliferation [17]. Similarly, graphene nanoplatelets embedded in a PDMS matrix have resulted in composites with expansion and contraction effects activated by near infrared (NIR) radiation [18, 19].

Polymer composites incorporating carbon allotropes have been widely explored for biomedical, chemical and engineering applications. Single-wall and multi-wall carbon nanotubes in PDMS (PDMS-SWCNTs, PDMS-MWCNTs) have shown to provide improved electrical, thermal, conductive or piezoresistive properties. Furthermore, the electrical and photomechanical actuation of carbon nanotubes (CNTs) have shown to be useful to fabricate polymer composites working as light triggered actuators yielding forces in the order of tens of kPa [18, 20]. More recently, micron-range deformations induced by light irradiation were also demonstrated in composites of PDMS and carbon nano powder [21].

Thus far, most of the work related to the production of materials with electrical or photomechanical actuation capabilities has been based on CNTs. However, the use of carbon soot particles (CSP) as a filler to produce low-cost photomechanical responsive composites has not been explored. CSP are nanospheres with varied internal structures of concentrically wrapped, graphene-like layers of carbon, and with grape-like (acinoform) morphologies [22]. They are generally considered as an unwanted byproduct from the incomplete combustion or pyrolysis of carbon based materials and thus very little is known about their performance as composites constituents. The aim of this work is to evaluate the performance of PDMS-CSP composites as an alternative smart material for converting light into mechanical energy, which may lead to the production of low-cost of photomechanical actuators, optically reconfigurable surfaces or optical actuating-sensing devices for engineering applications.

## 2. Experimental details

Pure PMDS and PDMS-CSP (1 and 3 % wt.) membranes were prepared following the procedure described by Shahzad et. al [23]. Briefly, the CSP were dispersed into the PDMS polymer using high speed mechanical stirring (1000 rpm for 10 min). Subsequently, the cross-linker

was added and this mixture was stirred for 5 min; the composite mix was further sonicated (37 KHz for 15 min.) at room temperature to get an homogeneous dispersion of the CSP. The resulting mix was disseminated on a polystyrene mold to obtain thin (100 to 1000 micrometers depending on the mold) composite membranes. Finally, these were degassed in vacuum to remove entrapped air bubbles in the matrix and then thermally cured at 70 °C for 4h, resulting in flexible and self standing composite samples.

Small strips of the composites were immersed in liquid nitrogen and subsequently fractured in order to observe their cross-section area by Field Emission Scanning Electron Microscopy (FE-SEM, Merlin Gemini II, Carl Zeiss). Improved FE-SEM imaging was achieved upon coating the samples with a thin layer of chromium deposited by sputtering. The structure of the composites was determined by X-ray diffraction analysis (Rigaku ULTIMA-IV diffractometer with a Cu  $K_{\alpha}$  radiation and  $\lambda = 1.5419\text{\AA}$ ). The chemical bonding of the composites was explored by Raman spectroscopy using an EnSpectr R532 Raman analyzer (200-4000  $\text{cm}^{-1}$  spectral range,  $\lambda = 532\text{nm}$ , 50mW and spot size= 45 ( $\pm 5$ ) and 25 ( $\pm 4$ )  $\mu\text{m}$  for 10X and 20X, respectively). In order to avoid potential thermal modification or damage of the composite surface, the laser probe beam was attenuated by 50%. The thermal stability and decomposition rate of the composites were obtained by thermogravimetric analysis (TGA) using an SDT Q600 thermobalance (TA Instruments), with an air mass flow rate of 100 mL/min and a temperature ramp rate of 10°C/min.

To evaluate the mechanical behaviour of the composite samples, dog-bone specimens were prepared following the ASTM D1708 standard. The thicknesses of the samples used for mechanical testing were measured with a digital micrometer (Mitutoyo) yielding the following values: PDMS 760 microns, PDMS 1% CSP 716 microns and PDMS 3% CSP 700 microns. The corresponding measured thickness for each sample was used to calculate the cross-section area required for the uniaxial tension and relaxation experiments. Uniaxial tensile experiments were carried out with a custom-designed device coupled to an optical microscope to perform digital image correlation analysis on the material surface as shown in Fig. 1. A strain velocity of 0.16 mm/s was used and the displacement, force and images were acquired, as function of time, in a synchronized manner through a virtual instrument programmed in LabVIEW. All the information was registered by a computer for further analysis. From the data of the uniaxial tensile tests, mechanical properties such as shear modulus, maximum stress, maximum stretch ratio and toughness of the composites were determined using the first-order Ogden model for uniaxial tension [24] given by the following equation:

$$\sigma(\lambda) = \frac{2 * \mu}{\alpha} * (\lambda^{(\alpha-1)} - \lambda^{(-\frac{1}{2}\alpha-1)}) \quad (1)$$

where  $\sigma$  is the stress (in Pa),  $\lambda$  is the stretch or elongation ratio (related to the classical definition of engineering strain as  $\lambda = \varepsilon + 1$  [25]),  $\mu$  is the shear modulus and  $\alpha$  is a parameter related to stretch invariants for incompressible materials according to the strain energy function [24]. Physically,  $\alpha$  is directly related to the alignment rate of the polymeric chains under uniaxial tension [24, 26]. If  $\alpha$  increases, the polymeric chains will be aligned at a lower stretch ratio. From the data of uniaxial tensile experiments and considering the Ogden model,  $\mu$  and  $\alpha$  can be easily estimated by non-linear fitting.

Once the elastic parameters  $\mu$  and  $\alpha$  of the composites were determined, their photomechanical responses were evaluated. In these experiments, the dog-bone sample was located between the grips of the mechanical tester; a small pre-load (0.7 N) was applied to avoid buckling on the composite surface as well as to keep the sample in place thereby reducing the entropy of the system because of the alignment of the polymeric chains. Subsequently, a continuous wave (CW) fiber-coupled diode laser (Thorlabs, 975 nm, 800 mW maximum output power) was used to irradiate the sample. On the other side of the sample, a CCD camera with proper optical

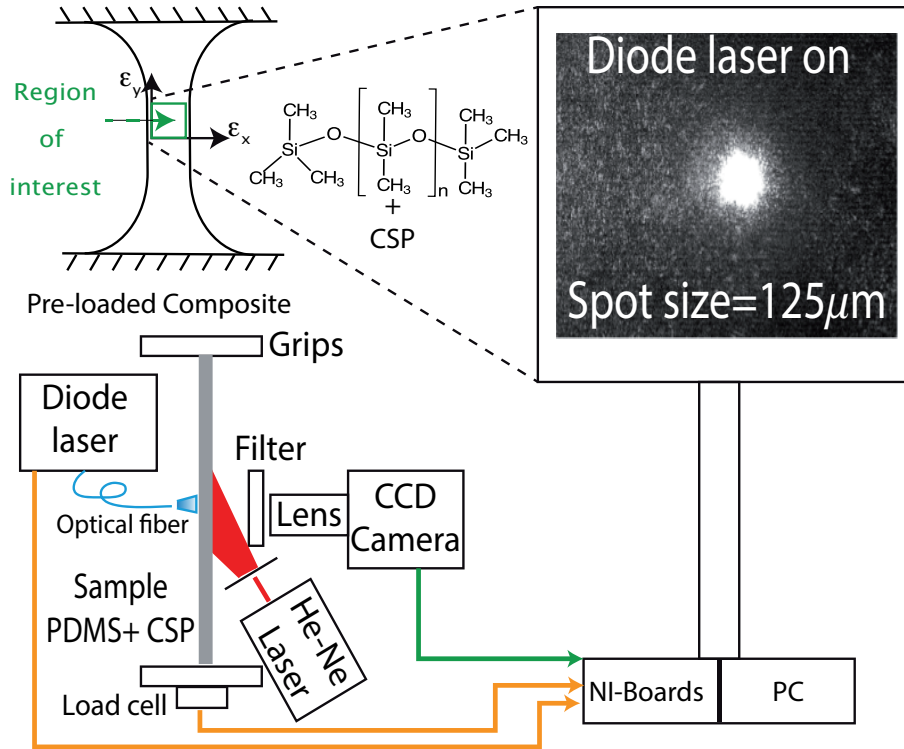


Fig. 1. Experimental setup to evaluate the opto-mechanical response of composites under infrared (IR) laser irradiation. The inset shows the chemical structure of the PDMS matrix hosting the CSP.

filters was coupled to the optical microscope to register the speckle pattern generated by the illumination of the expanded beam of a He-Ne laser. The speckle pattern was used in order to enhance the digital image correlation (DIC) process and then the in-plane strain. Using this setup, showed in Fig. 1, we were able to detect localized micro-deformations induced on the composite when the laser diode is on, owing to the interaction between light and the embedded CSP. The photo-induced micro-deformations can be further linked to the macromechanical response of the composite by means of a load cell, which allows to obtain a stress vs. time curve showing the effects of laser irradiation on the sample. These were registered as peaks on stress vs. time curve evidencing an increase on the  $\Delta\sigma_{light}$  stress due to strain induced by light. We estimated the magnitude of the optically induced stress as  $\Delta\sigma_{light} = \sigma_{LaserOff} - \sigma_{LaserOn}$ .

As shown in the following sections, laser irradiation of the sample produces both, macromechanical and micromechanical responses; while the latter is analyzed via DIC, the former is directly measured by the load cell of the mechanical tester. DIC analysis allows for the calculation of displacement vector fields from image pairs  $u_k(x_k, y_k)$  and  $v_k(x_k, y_k)$ . These are subsequently used to determine the in-plane strains by minimizing the errors of a six parameters linear model based on the following displacement equations [27, 28]:

$$u_k(x_k, y_k) = A_1 x_k + B_1 y_k + C_1 + \delta_u(x_k, y_k) \quad (2)$$

$$v_k(x_k, y_k) = A_2 x_k + B_2 y_k + C_2 + \delta_v(x_k, y_k) \quad (3)$$

The minimization process yields the values for the parameters A, B and C, related to the

in-plane strains as follows:  $A_1 = \epsilon_{xx}$  (strain in the  $x$  direction),  $B_2 = \epsilon_{yy}$  (strain in the  $y$  direction),  $\frac{1}{2}(B_1 + A_2) = \epsilon_{xy}$  (shear strain in the  $xy$  plane),  $\frac{1}{2}(B_1 - A_2) = \theta$  (rotation in the  $xy$  plane),  $T_x = C_1$  (translation in the  $x$  direction),  $T_y = C_2$  (translation in the  $y$  direction); finally,  $\delta_u(x_k, y_k)$  and  $\delta_v(x_k, y_k)$  represent the minimization parameters.

### 3. Results

The FE-SEM images are presented in Fig. 2; this set of images show the morphological features of pure PDMS and CSP Figs. 2(a) and 2(b), respectively. While the PDMS polymeric matrix shows a soft and continuous surface Fig. 2(a), the CSP image reveals grape-like clusters of nanospheres Fig. 2(b) which is the typical morphology reported for this material [22]. Figs. 2(c) and 2(d) show the cross-sectional area for PDMS 1% CSP and PDMS 3% CSP; in both cases, carbon soot clusters embedded in the polymeric matrix can be readily observed. The grape-like morphology of the CSP was still observed in the composites. Figs. 2(e) and 2(f) show the dispersion of the embedded CSP on the cross-section areas of PDMS 1% CSP and PDMS 3% CSP samples, respectively.

The X-Ray diffraction patterns of pure PDMS, PDMS-CSP(1% wt.) and PDMS-CSP(3% wt.) are shown in Fig. 3(a). The pattern of pure PDMS shows a broad amorphous peak ranging between  $11.5^\circ$  and  $12.1^\circ$ , which corresponds to the tetragonal crystal lattice of PDMS [17, 29]. The low-intensity peak located at  $2\theta=26.5^\circ$  corresponds to the embedded carbon soot particles of both PDMS samples with 1% wt and 3% wt. of CSP. This peak has been reported as graphite (JCPDS: 25-0284) by other authors and it can be attributed to the (002) plane of graphitized carbon [30–32]. In addition, the percentage of crystallinity of PDMS, PDMS-CSP(1% wt.) and PDMS-CSP(3% wt.) were 24, 19 and 27% respectively.

As seen in Fig. 3(b), the Raman spectrum of the pure CSP shows well defined peaks of carbon forms. These include the disordered D-band at  $1362\text{ cm}^{-1}$ , the graphitized G-band at  $1582\text{ cm}^{-1}$  and a 2nd order mode D'-band at  $2658\text{ cm}^{-1}$  [23]. The spectrum of pure PDMS, also shown in Fig. 3(b), presents the typical vibrational modes for silicon, carbon, oxygen and hydrogen bonds; these include symmetric stretching (Si-O-Si,  $488\text{ cm}^{-1}$ ), symmetric rocking ( $Si-CH_3$ ,  $621\text{ cm}^{-1}$ ), symmetric stretching (Si-C,  $708\text{ cm}^{-1}$ ), asymmetric stretching (Si-C) and asymmetric rocking ( $CH_3$ ) overlapping at  $787\text{ cm}^{-1}$ . Finally, the spectrum also shows the characteristic vibrational modes of the methyl group located within  $862$  and  $296\text{ cm}^{-1}$  [23, 33]. In contrast, for the PDMS-CSP composites, the Raman spectra is mainly dominated by the PDMS sharp features and the D and G bands are barely seen as those obtained for the pure CSP, Fig. 3(c). This can be attributed to their lower intensities compared to the molecular vibrations associated to the PDMS matrix.

Figure 3(d) shows the results of the thermogravimetric analysis (TGA), i.e., the thermal stability and decomposition rate in air of PDMS, CSP and the composites. For PDMS and its composites, the thermal decomposition starts within the  $300$  and  $350^\circ\text{C}$  temperature range; above this range, a drastic weight loss can be observed. Note that weight loss for pure CSP starts before these range; the corresponding weight loss percentage for these temperatures obtained from TGA analysis are summarized in Table 1.

In contrast to graphite ( $450$  to  $650^\circ\text{C}$  degradation temperature range) and CNTs (above  $600^\circ\text{C}$ ) [34], the CSP degradation (7 wt,%) starts at a lower temperature range ( $300$  to  $400^\circ\text{C}$ ). This may be due to moisture and the presence of amorphous carbon in these particles. The point of 50% weight loss in the TGA curve was obtained at  $525^\circ\text{C}$ , owing to the oxidation of graphitized carbon in the CSP, which remained until reaching  $800^\circ\text{C}$ . The remaining 13 wt. % of residual impurities is mainly due to high temperature, stable graphite and inorganic materials contained in CSP. Notice that the PDMS-CSP composites show equal or better thermal stability (from  $300$  to  $700^\circ\text{C}$ ) than that obtained separately for CSP as shown in Fig. 3(d) and Table 1.

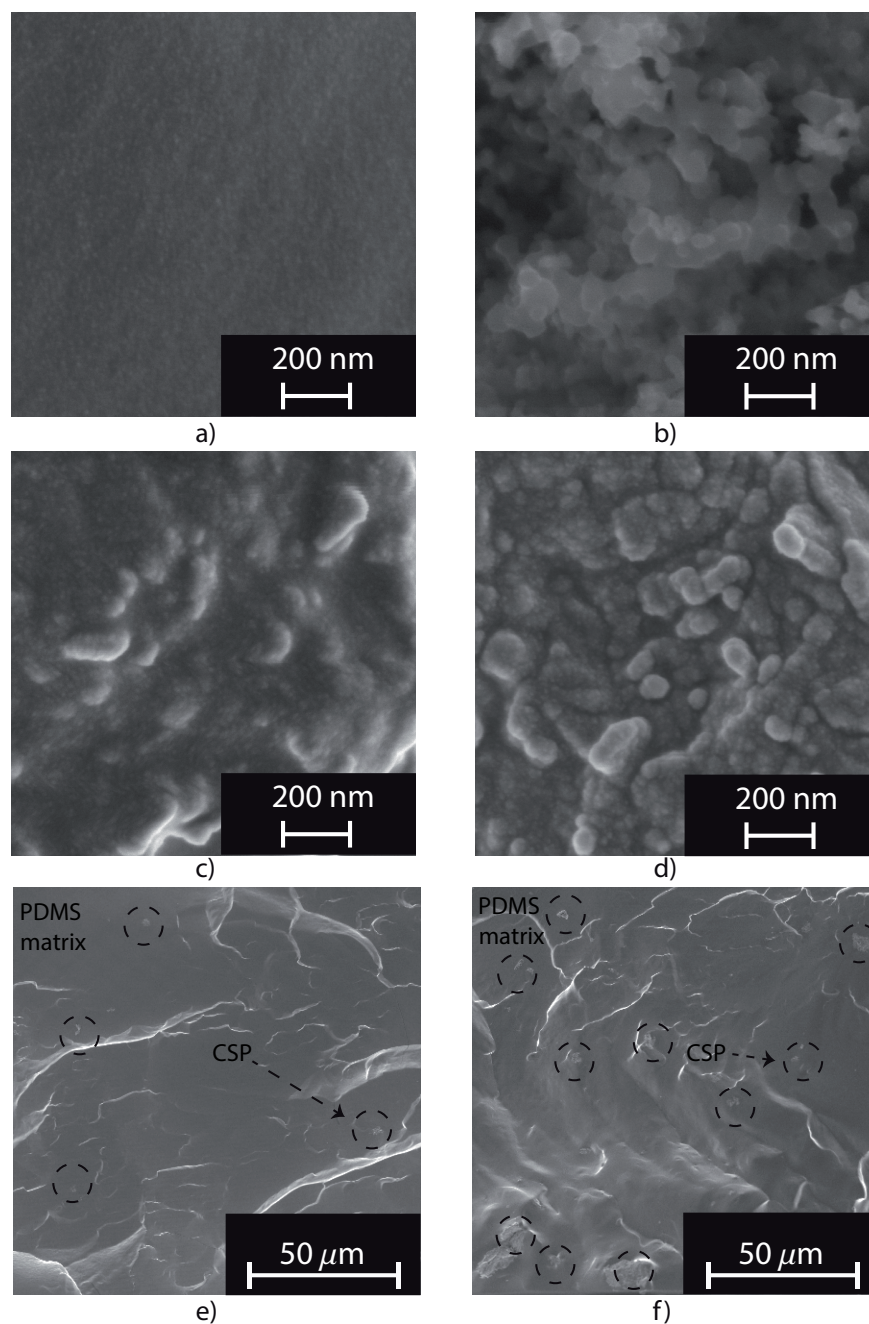


Fig. 2. FE-SEM images cross-section area of pure PDMS and composites. a) PDMS polymeric matrix showing a soft surface; b) Morphology of the filler showing clusters of carbon soot particles (CSP); c) Carbon soot cluster embedded into PDMS-CSP(1%wt.) sample; d) Carbon soot cluster embedded into PDMS-CSP(3%wt.) sample; e) Dispersion of carbon soot into PDMS-CSP(1%wt.) sample; f) Dispersion of carbon soot into PDMS-CSP(3%wt.) sample.

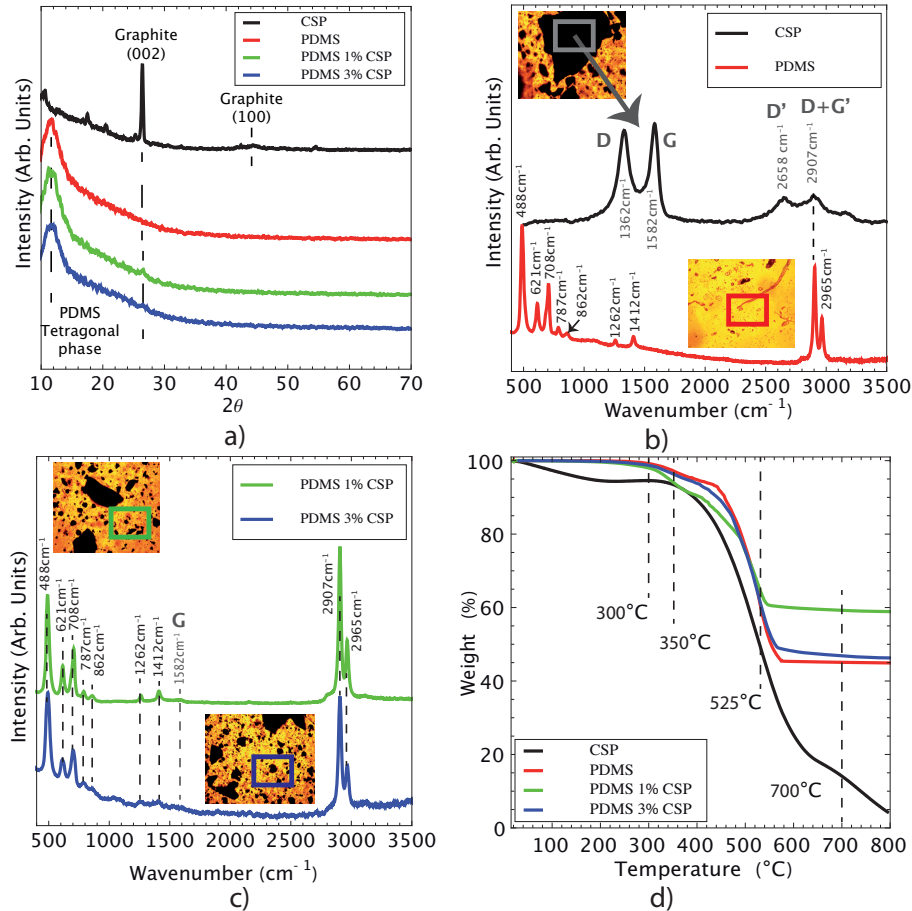


Fig. 3. Structural and thermal characterization of smart composites. a) X-Ray diffraction pattern of PDMS and PDMS-CSP; b) Raman spectra of pure PDMS and CSP; c) Raman spectra of PDMS-CSP composites; d) Thermal stability of PDMS, CSP and their composites.

The thermal stability becomes important for composites that are used as optical driven materials under IR irradiation. Its photomechanical behavior is based on the generation and transference of heat due to the capability of some carbon particles to absorb light and transfer the energy of excited electrons to vibrational modes within the atomic lattices, macroscopically rising the temperature [35]. According to TGA curves, our composites will be thermally stable below 300 °C; therefore, they can be useful as optically driven actuators involving highly localized temperature increments ranging between 100 and 150 °C [21].

The mechanical behaviour of the PDMS-CSP composites is shown in Fig. 4; as seen in the stress ( $\sigma$ ) vs. stretch ratio ( $\lambda$ ) curves, the composites exhibit an hyperelastic response for the uniaxial tension test, in accordance with previous reports for pure PDMS [36]. Clearly, the composites and pure PDMS show a rubber-like behaviour; we can therefore use the first-order Ogden model presented in Eq. (1) to fit the experimental data. The fitting process allows to obtain relevant mechanical parameters such as shear moduli, maximum stress, maximum stretch and toughness.

Figure 4(a) shows that the sample with 1% of CSP has better mechanical properties than pure

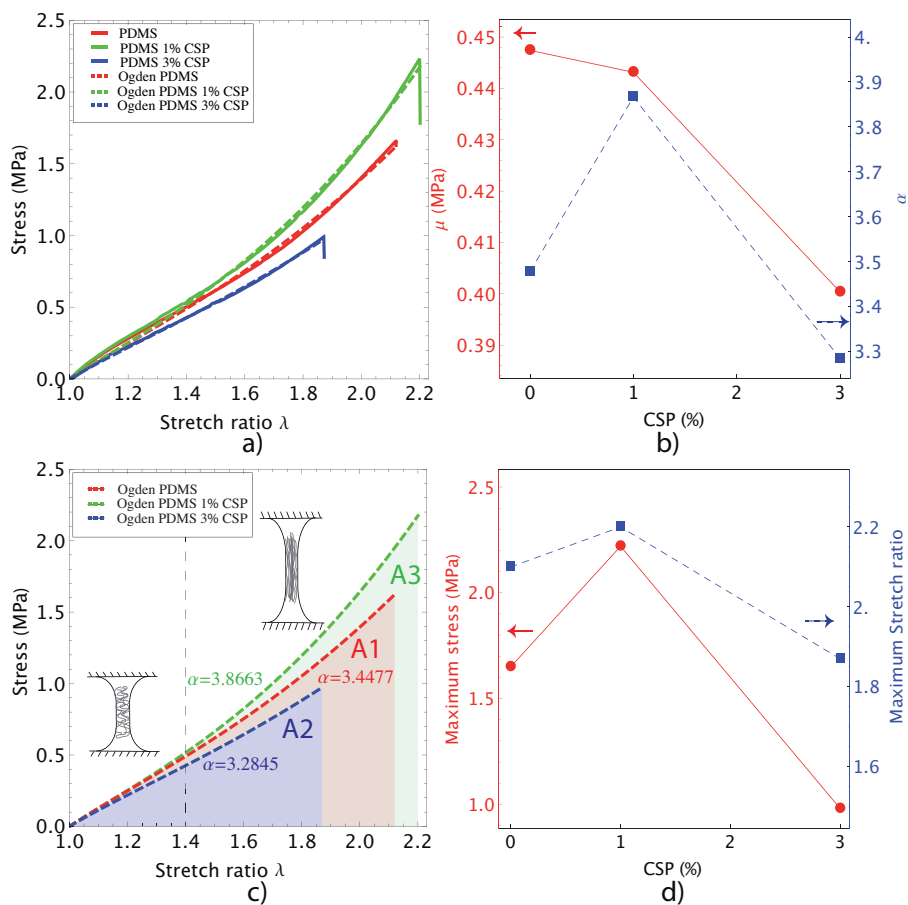


Fig. 4. Mechanical behaviour of the PDMS-CSP composites. a) Stress vs. stretch ratio curve showing the typical non-linear behaviour of hyperelastic materials; b) variation of elastic parameters as a function of CSP concentration; c) theoretical stress vs. stretch ratio curves, based on the Ogden model, used to evaluate the toughness of composites; d) Maximum stress and stretch ratio as a function of CSP concentration.

Table 1. Weight loss percentage as a function of temperature for CSP, PDMS and their composites (the values were obtained with respect to 100 wt.%).

Temperatures	300°C	350°C	525°C	700°C	Residue
$WeightLoss_{CSP}(\%)$	4	7	50	87	13
$WeightLoss_{PDMS}(\%)$	1	3	36	55	45
$WeightLoss_{PDMS1\%CSP}(\%)$	2	4	34	41	59
$WeightLoss_{PDMS3\%CSP}(\%)$	1.5	4	35	54	46

PDMS and PDMS-3% CSP. The addition of small quantities of CSP (1%) in the PDMS polymeric matrix thus increases the maximum stress and the maximum stretch by approximately 34.5% and 4.7%, respectively as it is shown in Fig. 4(d). In contrast, the shear modulus only shows a slight variation around the nominal value for PDMS when the CSP are incorporated into the matrix, Fig. 4(b). As with the other mechanical parameters, the values obtained for the shear modulus were in good agreement with those reported previously for pure PDMS [36].

As seen in Fig. 4(b), incorporation of CSP in PDMS yields changes in the elastic parameters  $\mu$  and  $\alpha$ . These are summarized in Table 2 along with their corresponding standard deviation. Notice that while only a slight reduction in the shear modulus  $\mu$  is observed with the addition of CSP, the parameter  $\alpha$  shows a maximum value for a concentration of 1% of CSP. The physical meaning of  $\alpha$  is related to the alignment rate of the polymeric chains during the uniaxial tension test; this is depicted in the insets shown in Fig. 4(c). In our experiments, stretch ratio values beyond 1.4 clearly showed the effects of polymer chain alignment for pure PDMS as well as for the PDMS-CSP composites. Notice that a concentration of 1% of CSP seems to favor a faster alignment of polymeric chains in comparison to the other samples. Now, considering the mechanical parameters  $\mu$  and  $\alpha$  presented in Table 2 and the Eq. (1), the mathematical models that mimic the non-linear mechanical behavior of PDMS and PDMS-CSP can be easily obtained. Hence, these can be integrated to obtain the corresponding toughness for each composite (i.e., areas A1, A2 and A3 shown in Fig. 4(c)). The toughness values resulting from integration of Eq. (1), using the corresponding fitting parameters for each composite, were  $0.8274 \cdot 10^6$ ,  $1.0978 \cdot 10^6$  and  $0.4103 \cdot 10^6$  ( $J \cdot m^{-3}$ ) for PDMS, PDMS 1% CSP and PDMS 3% CSP; respectively. Notice that the addition of 1% of CSP produces a more elastic and resistant material than PDMS and PDMS with 3% CSP. Although further work is required to fully understand this result, a possible explanation for the early fracture of the PDMS 3% CSP samples could be that at this concentration, the particles may act as stress concentration points.

Table 2. Mechanical parameters of the PDMS-CSP composites.

Sample	$\mu$ (MPa)	$\pm$ Std. Error	$\alpha$	$\pm$ Std. Error
PDMS	0.4474	0.0017	3.4777	0.0101
PDMS 1% CSP	0.4431	0.0018	3.8663	0.0093
PDMS 3% CSP	0.4003	0.0008	3.2845	0.0079

We finally show the results for the photomechanical response of the PDMS-CSP composites. This response is based on light absorption (IR irradiation) by CSP that causes heat percolation into the PDMS polymeric matrix; as a result, changes of entropic elasticity were registered producing a contraction force on the preloaded composite. Figure 5(a) shows the stress as a

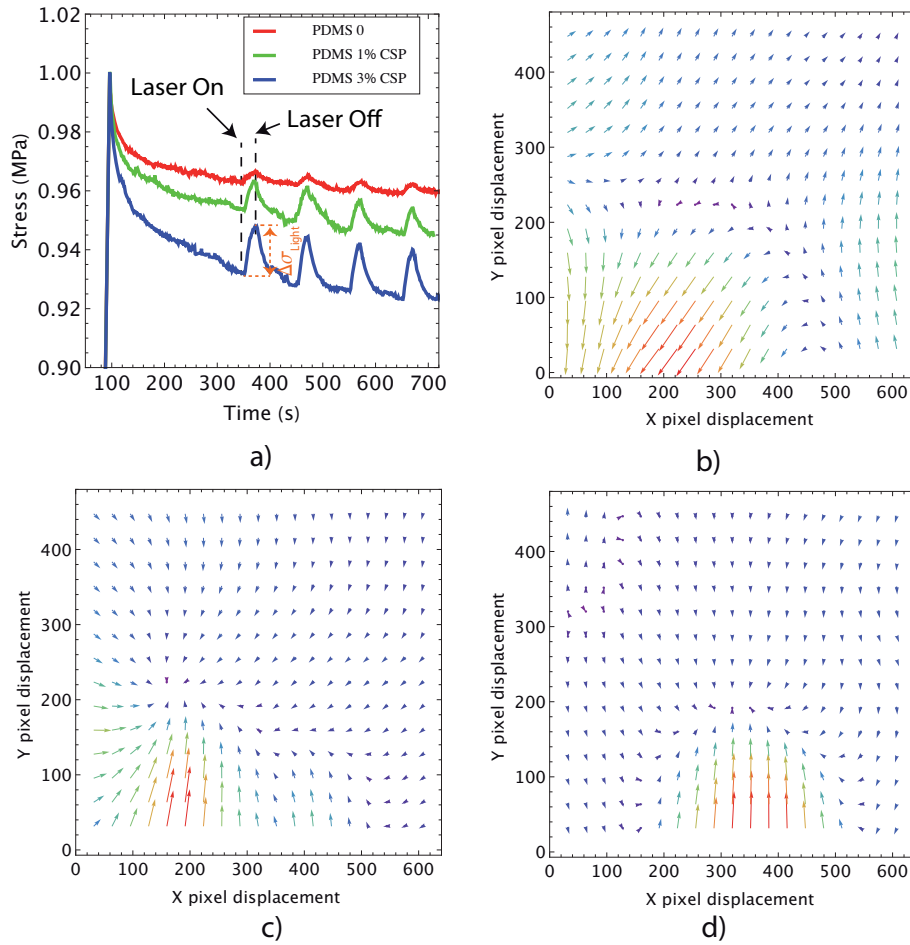


Fig. 5. Photomechanical response of the PDMS-CSP composites. a) Photomechanical response of preloaded PDMS and its composites under infrared (IR) laser irradiation (550 mW); b) displacement vector field for pure PDMS under IR irradiation; c) displacement vector field for PDMS 1% CSP under IR irradiation; and d) displacement vector field for PDMS 3% CSP under IR irradiation.

function of time curve of PDMS samples and its composites under IR irradiation pulses. It is clear that when the IR diode laser is switched on, the stress increases notoriously for the composites; in addition, it was found that this behaviour is reversible when the laser is switched off, as seen in the Fig. 5(a) showing the response of the composite to a cyclic exposure to the IR radiation. Upon comparing Figs. 5(b)-(d), the differences in photomechanical response for the tested samples are evident. The displacement vector field obtained for pure PDMS, Fig. 5(b), shows a predominantly shear strain component. In contrast, the addition of CSP in the polymeric matrix yields a contraction-like displacement vector field, Figs. 5(c) and (d); hence, the state of strain is changed under laser irradiation for the PDMS 1% CSP and PDMS 3% CSP composites showing  $\epsilon_{xx}$  and  $\epsilon_{yy}$  as the predominating strain components. The microstrain locally induced by laser irradiation was also observed and the load cell registered the corresponding induced force. This measurement together with the corresponding cross-sectional area of the samples were used to estimate the magnitude of the stress ( $\Delta\sigma_{light}$ ) produced by the optically induced strain; averages for these parameters resulting from data shown in Fig. 5 are summarized in Table 3. As observed in PDMS composites with carbon nanopowder [21], the PDMS-CSP samples are readily deformed by infrared irradiation within a micron-range. Furthermore, the load cell measurements provide evidence of the load capacity of the tested composites.

Table 3. Micromechanical behavior of the PDMS-CSP composites under infrared irradiation (550 mW).

Sample	$\epsilon_{xx} * 10^{-6}$	$\epsilon_{yy} * 10^{-6}$	$\epsilon_{xy} * 10^{-6}$	Stress induced by light (kPa)
PDMS	$-17 \pm 2$	$469 \pm 27$	$379 \pm 16$	$3.25 \pm 0.4$
PDMS 1% CSP	$-1341 \pm 88$	$-2854 \pm 120$	$-340 \pm 75$	$10 \pm 1$
PDMS 3% CSP	$-285 \pm 80$	$1390 \pm 108$	$74 \pm 7$	$16 \pm 0.5$

Further optical characterization of the samples included transmittance measurements using a UV-Vis spectrophotometer (Schimadzu 1800). Following the Beer-Lambert relation, we estimated the extinction coefficient for the samples as  $\beta = -(1/L) * Ln(I/I_0)$  where  $(I/I_0)$  is the transmittance and  $L$  is the thickness of the membrane. Figure 6(a) shows the resulting extinction coefficient as a function of wavelength for PDMS and its composites; the corresponding sample thicknesses for these measurements were 1032 microns (PDMS), 612 microns (PDMS 1% CSP) and 375 microns (PDMS 3% CSP). Hence, the extinction lengths for each sample are 8.35 (PDMS), 0.49 (PDMS 1% CSP) and 0.152 (PDMS 3% CSP), all of them in mm. Note that the samples may also produce light scattering, which is also accounted for in the resulting extinction lengths. Using these values, we can estimate the heating volumes considering an irradiation area of  $0.012 \text{ mm}^2$  (laser spot diameter of 125 microns) 0.10 (PDMS), 0.006 (PDMS 1% CSP) and 0.0018 (PDMS 3% CSP), all of them in  $\text{mm}^3$ . Clearly, the samples with CSP present a higher extinction compared to that of pure PDMS leading to increased thermal effects. These have been further shown to be highly localized and dependent on the concentration of absorbers in similar polymer composites [35]. This indicates that the laser induced strain is also highly localized, causing a more evident contraction within the composite polymeric matrix.

A more detailed analysis of the photomechanical response was performed upon evaluating the stress as a function of time for different laser powers. As before, the laser was turned on and off at different times and the  $\Delta\sigma_{light}$  was registered for the three samples. As seen in Fig. 6(b), an increase in laser power leads to a larger photomechanical response. Furthermore, a plot of the stress produced by the optically induced strain shown in Fig. 6(c) provides evidence of

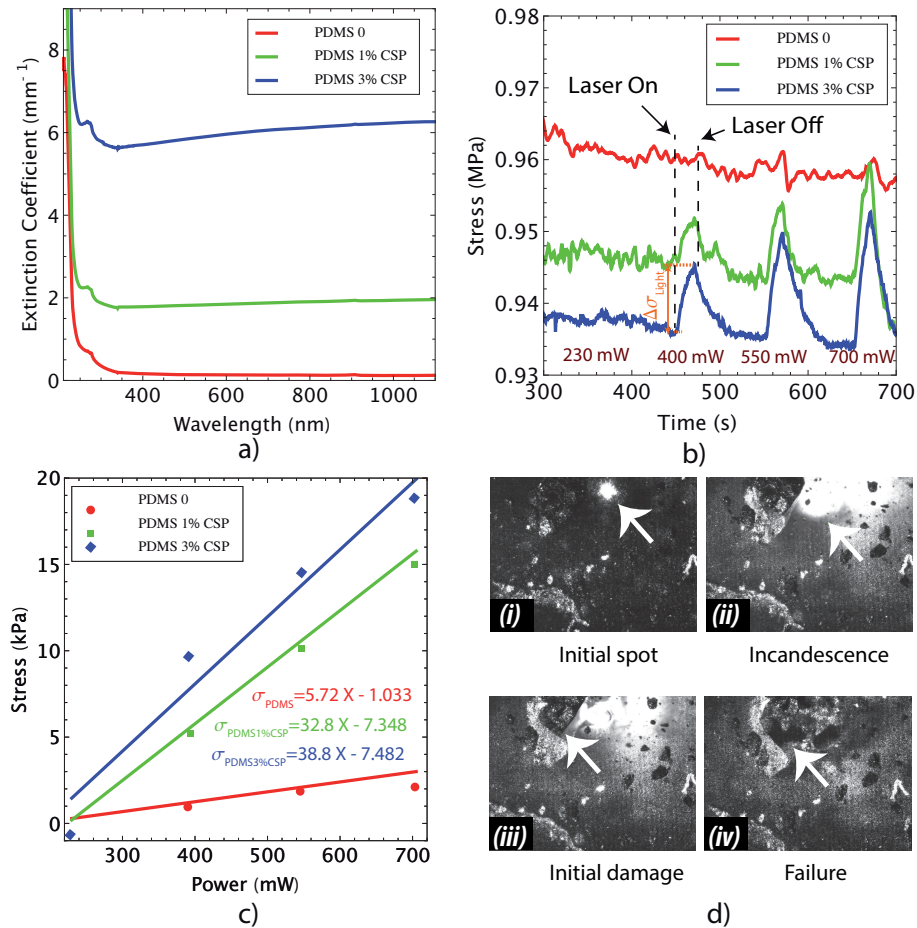


Fig. 6. Optical interaction between diode laser beam and PDMS composites. a) Extinction coefficient as a function of wavelength of PDMS and its composites. b) Stress as a function of time for different powers of diode laser showing activation (400 mW) and damage (700 mW) thresholds. c) Photomechanical response as a function of power and d) Images showing damage threshold at 700mW for composites (Visualization 1).

a linear photomechanical response as a function of optical power for all the samples. Notice also that the sample with a higher concentration of particles (PDMS 3% CSP) yields the most efficient conversion of IR irradiation into mechanical energy. Two other important features of the samples obtained from this analysis are the thresholds for activation and damage for the composites. We experimentally observed a power threshold below 400mW for the photomechanical response, although lower powers are predicted by the linear fittings of the stress vs. power curves. The damage of the samples occurred at 700mW for an exposure time of 20 seconds. A set of images in Fig. 6(d) illustrates the initial spot (i) at 700mW, just a few seconds after the incandescence of the sample (ii) occurs; subsequently, initial damage of the sample is clearly observed (iii) and finally, failure (iv) occurred leading to membrane rupture. Clearly, several parameters are to be optimized in order to obtain an optimal photomechanical response from this type of composites. In particular, the photothermal features of the membranes seem to be an important optimization parameter that may lead to improved photomechanical perfor-

mance [35]. Nonetheless, the proposed smart composites could render useful as photoactuators with a load capacity ranging between 10 and 16 kPa. This provides good evidence that CSP composites can offer a comparable performance to CNTs composites, and thereby offering a low-cost alternative for producing smart polymer composites.

#### 4. Conclusions

Smart composites based on PDMS and carbon soot particles were obtained and their mechanical features were fully characterized. A photomechanical response of these materials was demonstrated showing that a mechanical force is locally induced under IR laser irradiation. The PDMS 1% CSP composite exhibited the best mechanical properties of all the tested samples, showing improved thermal stability compared to pure PMDS and PDMS 3% CSP. Adding 1% wt. and 3% wt. of CSP into PDMS polymeric matrix enhanced the photomechanical response by 3 and 5 times, respectively. The load capacity of these materials, ranging from 10 to 16 kPa, seems to be promising for developing optically driven actuators, optically reconfigurable surfaces and optical actuating-sensing devices based on PDMS-CSP composites.

#### Acknowledgments

This work was developed with the financial support from PAPIIT DGAPA-UNAM program through grants *IT100215*, *IT101215*; Photocatalytic Systems for Clean Energy and Environment Applications (*PhocsCleenEU318977*) and the International Academic Mobility Program of UNAM (*COIC – STIA – 235*). The authors are grateful to Dr. Mauro Raimondo (Politecnico di Torino) for the FE-SEM images, Dra. Adriana Tejada for X-Ray measurements (IIM-UNAM) and MSc. Damaris Cabrera for the TGA and DSC analyses (IIM-UNAM).